

## Article

# Computational Design of Gas Sensors Based on V<sub>3</sub>S<sub>4</sub> Monolayer

Ilya V. Chepkasov <sup>1</sup>, Ekaterina V. Sukhanova <sup>2</sup> , Alexander G. Kvashnin <sup>1,\*</sup> , Hayk A. Zakaryan <sup>3</sup> , Misha A. Aghamalyan <sup>3</sup> , Yevgeni Sh. Mamasakhlisov <sup>4,5</sup>, Anton M. Manakhov <sup>6</sup> , Zakhar I. Popov <sup>2</sup>  and Dmitry G. Kvashnin <sup>2</sup> 

<sup>1</sup> Center for Energy Science and Technology, Skolkovo Institute of Science and Technology, Bolshoy Boulevard 30, bld. 1, 121205 Moscow, Russia; i.chepkasov@skoltech.ru

<sup>2</sup> Emanuel Institute of Biochemical Physics RAS, 4 Kosygin Street, 119334 Moscow, Russia; yekaterina.sukhanova@phystech.edu (E.V.S.); zipcool@bk.ru (Z.I.P.); dgkvashnin@phystech.edu (D.G.K.)

<sup>3</sup> Computational Materials Science Laboratory at the Center of Semiconductor Devices and Nanotechnology, Yerevan State University, 1 Alex Manoogian St., Yerevan 0025, Armenia; hayk.zakaryan@ysu.am (H.A.Z.); misha.aghamalyan@gmail.com (M.A.A.)

<sup>4</sup> Department of Molecular Physics, Yerevan State University, 1 Alex Manoogian St., Yerevan 0025, Armenia; y.mamasakhlisov@ysu.am

<sup>5</sup> Department of Materials Technology and Structure of Electronic Technique, Russian-Armenian University, 123 Hovsep Emin St., Yerevan 0051, Armenia

<sup>6</sup> Aramco Innovations LLC, Aramco Research Center, 119234 Moscow, Russia; anton.manakhov@aramcoinnovations.com

\* Correspondence: a.kvashnin@skoltech.ru



**Citation:** Chepkasov, I.V.; Sukhanova, E.V.; Kvashnin, A.G.; Zakaryan, H.A.; Aghamalyan, M.A.; Mamasakhlisov, Y.S.; Manakhov, A.M.; Popov, Z.I.; Kvashnin, D.G. Computational Design of Gas Sensors Based on V<sub>3</sub>S<sub>4</sub> Monolayer. *Nanomaterials* **2022**, *12*, 774. <https://doi.org/10.3390/nano12050774>

Academic Editors: Filippo Giannazzo and Ivan Shtepliuk

Received: 2 February 2022

Accepted: 22 February 2022

Published: 25 February 2022

**Publisher's Note:** MDPI stays neutral with regard to jurisdictional claims in published maps and institutional affiliations.



**Copyright:** © 2022 by the authors. Licensee MDPI, Basel, Switzerland. This article is an open access article distributed under the terms and conditions of the Creative Commons Attribution (CC BY) license (<https://creativecommons.org/licenses/by/4.0/>).

**Abstract:** Novel magnetic gas sensors are characterized by extremely high efficiency and low energy consumption, therefore, a search for a two-dimensional material suitable for room temperature magnetic gas sensors is a critical task for modern materials scientists. Here, we computationally discovered a novel ultrathin two-dimensional antiferromagnet V<sub>3</sub>S<sub>4</sub>, which, in addition to stability and remarkable electronic properties, demonstrates a great potential to be applied in magnetic gas sensing devices. Quantum-mechanical calculations within the DFT + U approach show the antiferromagnetic ground state of V<sub>3</sub>S<sub>4</sub>, which exhibits semiconducting electronic properties with a band gap of 0.36 eV. A study of electronic and magnetic response to the adsorption of various gas agents showed pronounced changes in properties with respect to the adsorption of NH<sub>3</sub>, NO<sub>2</sub>, O<sub>2</sub>, and NO molecules on the surface. The calculated energies of adsorption of these molecules were −1.25, −0.91, −0.59, and −0.93 eV, respectively. Obtained results showed the prospective for V<sub>3</sub>S<sub>4</sub> to be used as effective sensing materials to detect NO<sub>2</sub> and NO, for their capture, and for catalytic applications in which it is required to lower the dissociation energy of O<sub>2</sub>, for example, in oxygen reduction reactions. The sensing and reducing of NO<sub>2</sub> and NO have great importance for improving environmental protection and sustainable development.

**Keywords:** 2D; nanomaterials; vanadium chalcogenides; monolayer; gas sensor; dft

## 1. Introduction

The gas-sensing system is important in various applications including industrial pollutant gas leakage detection, environmental monitoring, medical care, food industry, etc. [1]. Nanomaterials show great performance in this field of technology [2]. Nowadays, the most effective materials for gas sensing belong to the groups of metal-organic framework-based nanostructured materials [3,4] and low-dimensional materials [5,6]. Another type of sensor is based on magnonic sensors with the presence of magnetic nanoparticles [7] and two-dimensional materials [1,8] and it seems to be promising for further development.

Magnetic gas sensors are characterized by greater safety of use, lower working temperatures, and faster response times than traditional gas sensors based on the variation of

electronic properties. The change in the magnetic properties of the active material can be detected, for example, by the Hall effect observation, change in magnetization or electron spin orientation, ferromagnetic resonance modification, magneto-optical Kerr effect, and magneto-static wave oscillation effect [9,10].

Two-dimensional materials that belong to the family of transition metal dichalcogenides (TMD) have attracted great interest in the field of gas sensors due to a large surface-to-volume ratio, leading to specific electrical properties. These properties can be strongly modified by the surface adsorbates [11], which is confirmed by recent theoretical studies ( $\text{MoS}_2$  [12],  $\text{SnS}_2$  [13], and  $\text{VS}_2$  [14]). However, there is still a lack of critical information about the real possibility of using TMD monolayers as a magnetic gas sensor component. Most known TMDs are non-magnetic [15,16], but it was shown [17–22] that adding point defects or adsorption of non-metallic elements can make them magnetic.

Among the TMD family, the  $\text{VS}_2$  monolayer has attracted particular interest due to its intrinsic magnetism [23–25] which can be tuned by, for example, tensile strain [26]. Ferromagnetism in the  $\text{VS}_2$  layer was experimentally confirmed at room temperature by Gao et al. [23] where an unusual hybridization of  $3d$  orbitals of V and  $3p$  orbitals of S was also observed. Zhong et al. [27] determined that Curie temperature ( $T_c$ ) strongly depends on the thickness, and the  $T_c$  of single-layer  $\text{VS}_2$  was determined to be 72 K.

Despite the extensive study of  $\text{VS}_2$ , there is still an open question related to the study of 2D monolayers in the V–S system with compositions differing from  $\text{VS}_2$ . Recent studies have shown that in M–X systems (M = W, Mo, etc.; X = S, Se, Te, etc.), new two-dimensional and non-stoichiometric structures can be formed [28]. There are several studies devoted to vanadium sulfide crystals such as  $\text{VS}_4$  [29,30],  $\text{V}_3\text{S}_4$  [31,32],  $\text{V}_5\text{S}_4$  [33],  $\text{V}_5\text{S}_8$  [34], and  $\text{V}_3\text{S}$  [35] structures in different applications. For example, the bulk  $\text{V}_3\text{S}_4$  usually forms a distorted NiAs-type structure with single-layer  $\text{VS}_2$  building blocks and additional V atoms bonded between two layers with metallic characteristics [36]. Since the properties of two-dimensional materials differ from the bulk ones, this significantly expands the scope of their application. Motivated by the above-mentioned facts, we performed a complex investigation toward designing new two-dimensional V–S phases suitable for magnetic gas sensors. Among the considered earlier structures, we predicted a novel magnetic  $\text{V}_3\text{S}_4$  monolayer demonstrating stability as promising for applications as an element of CO and NO molecule magnetic gas sensors.

## 2. Materials and Methods

The global search for thermodynamically stable 2D compounds in the V–S system was performed by using the variable-composition evolutionary crystal structure prediction algorithm USPEX [37–39]. The first 180 structures (first generation) were generated by the operator of random symmetry [39] in the unit cell with up to 16 atoms in the primitive cell. Further generations (120 structures in each) consisted of 20% of the structures of random symmetry [39] and 80% of the structures were generated by the operators of heredity, soft mode mutation, and transmutation.

For each considered compound, the structure was optimized using density functional theory (DFT) [40,41]. The generalized gradient approximation (GGA) was used with the Perdew–Burke–Ernzerhof (PBE) parameterization for the exchange-correlation functional [42] as implemented in the Vienna Ab initio Simulation Package (VASP) 6.1.2 [43–46]. Ion-electron interaction was described by the augmented plane waves method (PAW) [47], and the cutoff energy of plane waves was set to 500 eV. The partition of the first Brillouin zone into a grid of k-points was carried out within the Monkhorst–Pack scheme [48] with a resolution of  $2\pi \times 0.05 \text{ \AA}^{-1}$ . To consider strong electron correlations between the localized  $3d$ -electrons of V atoms, the GGA +  $U$  approach in Dudarev's formulation [49,50] was applied, where the values of parameter  $U_{\text{eff}} = U - J$  varied from 0 to 4 eV. The Grimme corrections (DFT-D3) [51] were applied to take into account van der Waals interactions between the  $\text{V}_3\text{S}_4$  surface and molecules.

The phonon density of states for  $V_3S_4$  was calculated using the finite displacements method as implemented in the PHONOPY program package (version 2.11.0) [52,53] with forces computed by VASP [43–46]. For phonon calculation, the  $4 \times 2 \times 1$  supercell was used. Phonon dispersion curves were plotted using sumo software (version 2.2.5) [54].

### 3. Results and Discussion

#### 3.1. Crystal Structure Prediction

Two-dimensional compounds in the V-S system were predicted by using the variable-composition evolutionary search as implemented in USPEX [37–39] code. The V-S system belongs to strongly correlated systems. Consequently, it is necessary to use the GGA +  $U$  approach to correctly describe the stability and electronic properties of V-S compounds, as suggested in [55,56]. As we considered many different compositions and structure types in a single evolutionary search, we could not use one specific  $U_{eff}$  value. Thus, we performed five independent evolutionary searches with different  $U_{eff}$  values from 0 to 4 eV with the step of 1 eV and the resulting convex hulls are summarized in Figure 1. Besides pure compounds, we predicted four thermodynamically stable monolayers with various compositions, namely,  $V_3S$ ,  $VS$ ,  $V_3S_4$ , and  $VS_2$  (see Figure S1 and Table S1). In the resulting convex hull H, polymorphic modification of  $VS_2$  becomes less energetically favorable than the T phase at the  $U_{eff}$  value  $>2$  eV, which is consistent with a previous study by Zhuang et al. [55]. At the same time,  $VS_2$  and  $VS$  composition disappeared from the convex hull at the  $U_{eff}$  value equal to 4 eV and 3 eV, respectively.  $V_3S_4$  and  $V_3S$  phases were thermodynamically stable at all considered  $U_{eff}$  parameter values. For all further calculations, we finally employed the value of  $U_{eff} = 3$  eV [55].

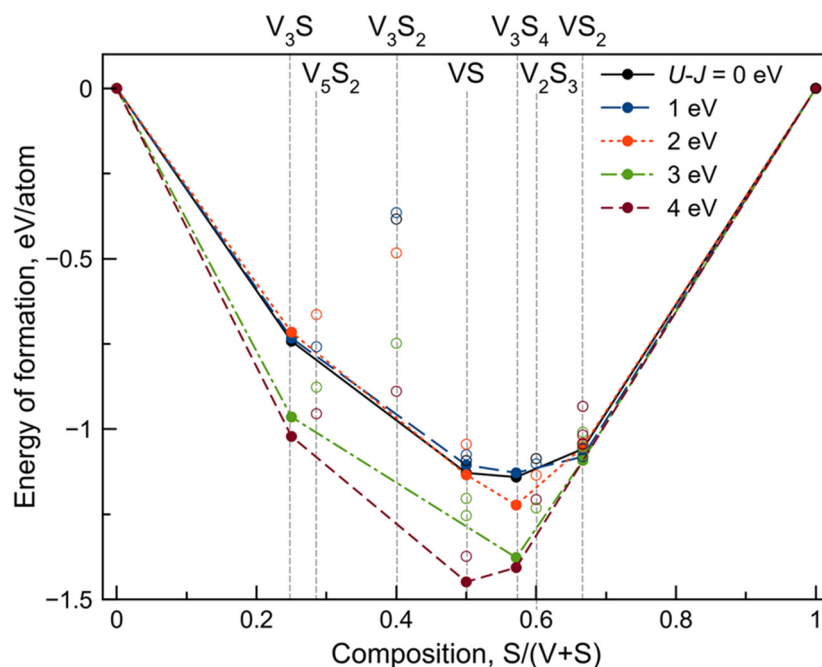


**Figure 1.** Calculated convex hulls of the V-S system with different  $U_{eff}$  values.

#### 3.2. Novel $V_3S_4$ Phase

We predicted a novel monolayer structure of  $V_3S_4$  that was thermodynamically stable at all considered  $U_{eff}$  values (see Figures 1 and S1). This result was proved by an additional fixed-composition evolutionary search of  $V_3S_4$  that showed that the obtained structure had the lowest formation energy among other structures with the same composition. Detailed information is presented in the Supplementary Materials. Top and side views of the atomic structure of the novel  $V_3S_4$  phase are shown in Figure 2a. The  $V_3S_4$  phase has the cell parameters of  $a = 3.35$  Å,  $b = 6.75$  Å, and  $\gamma = 104.35^\circ$ . The unit cell of the  $V_3S_4$  monolayer

consists of three vanadium atoms, among which one atom exists in octahedral surroundings of sulfur atoms (marked by blue in Figure 2a), and two other vanadium atoms exist in a square pyramidal surrounding ( $C_{4v}$ ) as marked by green in Figure 2a. Suddenly, one can find analogies of  $V_3S_4$  monolayer in bulk crystals [57] in which alternation of structural elements of square pyramidal and octahedrally coordinated vanadium atoms are presented. Moreover, the exfoliation of the  $V_3S_4$  crystal from [33] along the  $[20\bar{1}]$  direction could give a monolayer with the same structure as predicted in our USPEX calculations. Thus, it can be assumed that the presence of a two-dimensional monolayer counterpart of the bulk crystals provides prerequisites for their experimental synthesis.

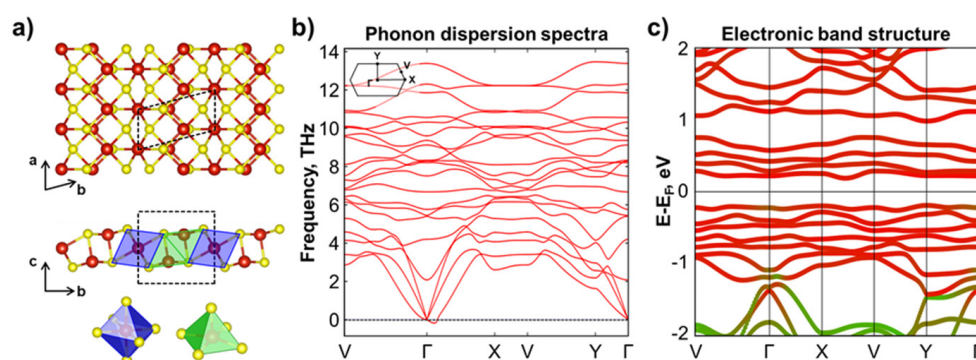


**Figure 2.** Newly predicted  $V_3S_4$  monolayer: (a) top and side views of the atomic structure (color legend: V—red; S—yellow); (b) phonon band structure; (c) electronic band structure of the most energetically favorable AFM configuration. The contributions from vanadium and sulfur atoms are indicated with red and green colors, respectively.

The dynamical stability of the predicted  $V_3S_4$  monolayer was studied by calculations of the phonon band structure as shown in Figure 2b. There are minor imaginary modes in the vicinity of the  $\Gamma$ -point in the obtained spectra usually associated with out-of-plane vibrational modes caused by the small supercell size, and therefore, we can conclude the dynamic stability of the predicted novel structure.

To examine in detail the electronic and magnetic properties of the  $V_3S_4$  phase, we first determined the monolayer's magnetic ground state. For this aim, we considered the  $2 \times 1 \times 1$  supercell of the  $V_3S_4$  phase in the ferromagnetic (FM) and 10 different antiferromagnetic (AFM) configurations (for more details, see Figure S2 in Supplementary Materials). The comparison of the total energies of these magnetic configurations is shown in Table S2 (Supplementary Materials). The most energetically favorable configuration was noted as AFM10 and the energy difference between the FM and AFM10 configuration was 0.15 eV per unit cell, which is relatively large, indicating the stability of antiferromagnetic configuration. The electronic band structure for the ground state calculation is presented in Figure 2c. Vanadium atoms in octahedral surroundings have a magnetic moment equal to  $1.97 \mu B$ , while vanadium atoms in the square pyramidal surrounding have a magnetic moment of  $2.14 \mu B$ . The novel  $V_3S_4$  monolayer in the AFM magnetic state exhibited semiconducting properties with the band gap of 0.36 eV.

The main feature of  $V_3S_4$  is the existence of two symmetrically inequivalent vanadium atoms. Furthermore, and more importantly, vanadium atoms in square pyramidal surroundings have a vacant  $d$ -orbital that can form a bond with different ligands; for example, with gas molecules, and depending on the binding characteristic, it should lead to a change in cleavage after binding to a gas molecule. This will affect the change in the electronic properties of  $V_3S_4$ , thus, the surface of the  $V_3S_4$  monolayer is promising as a gas sensor with a large number of adsorption centers.

### 3.3. Sensing Properties

A study of  $\text{V}_3\text{S}_4$  as a potential gas sensor was performed for the cases of the adsorption of CO,  $\text{CO}_2$ , NO,  $\text{NO}_2$ ,  $\text{NH}_3$ ,  $\text{H}_2\text{O}$ , and  $\text{O}_2$  molecules. For this study, the  $4 \times 2 \times 1$  supercell of  $\text{V}_3\text{S}_4$  was considered containing 24 vanadium and 32 sulfur atoms. For each molecule, a various number of possible adsorption sites were considered. The most energetically favorable sites for all molecules correspond to the vanadium atom of the outer layer in the square pyramidal surrounding (see Figure S3 in the Supplementary Materials).

Detailed information on the adsorption of different gas molecules on  $\text{V}_3\text{S}_4$  nanosheet is presented in Table 1. The energy of adsorption ( $E_a$ ) was calculated as  $E_a = E[\text{V}_3\text{S}_4 + \text{molecule}] - E[\text{V}_3\text{S}_4] - E[\text{molecule}]$ , where  $E[\text{V}_3\text{S}_4 + \text{molecule}]$  is the energy of the system consisting of the interacting  $\text{V}_3\text{S}_4$  monolayer and gas molecule, and  $E[\text{V}_3\text{S}_4]$  and  $E[\text{molecule}]$  are the total energies of the  $\text{V}_3\text{S}_4$  nanosheet and pristine molecule, respectively. Considering the sign of the charge transferred to the  $\text{V}_3\text{S}_4$  monolayer, we can conclude that CO,  $\text{CO}_2$ , NO,  $\text{NO}_2$ , and  $\text{O}_2$  molecules act as p-type dopants, while  $\text{NH}_3$  and  $\text{H}_2\text{O}$  molecules act as n-type dopants, as indicated by the positive sign of  $\Delta q$  (see Table 1). In systems with strong charge overflow such as in the cases of  $\text{O}_2$ , NO, and  $\text{NO}_2$  molecules, the sorption of extra electrons at the molecule leads to the occupation of antibonding orbitals increasing the molecule bond length (see Table 1). High values of adsorption energies, except for the  $\text{CO}_2$  molecule, are related to the pronounced charge redistribution in the interface area. However, in the case of the  $\text{CO}_2$  molecule, the obtained values of  $E_a$  and  $D$  and nearly zero charge redistribution suggest weak van der Waals interactions between the molecule and monolayer.

**Table 1.** Characteristics of the most energetically favorable adsorption sites in the  $\text{V}_3\text{S}_4$  nanosheet with different molecules adsorbed to the surface.  $E_a$  is the energy of adsorption;  $D$  is the perpendicular distance between molecule and adsorption site (V atom);  $\alpha_0$  and  $\alpha$  are the bond angles in V-shaped molecules before and after adsorption;  $d_0$  and  $d$  are the molecules bond lengths before and after adsorption; and  $\Delta q$  is the change in charge of the molecule between states before and after adsorption (within the Bader theory calculation [58,59]).

Molecule	$E_a$ (eV)	$D$ (Å)	$\alpha_0$ (°)	$\alpha$ (°)	$d_0$ (Å)	$d$ (Å)	$\Delta q$ (e)
CO	-0.82	2.11	-	-	1.14	1.14	0.069
$\text{CO}_2$	-0.26	2.39	179.97	179.48	1.17	1.17	0.007
$\text{H}_2\text{O}$	-0.83	2.23	104.35	106.48	0.97	0.97	-0.051
$\text{O}_2$	-0.59	2.04	-	-	1.23	1.32	0.473
$\text{NH}_3$	-1.25	2.22	106.58/106.57/106.56	108.49/108.63/107.59	1.02	1.02	-0.114
NO	-0.93	1.87	-	-	1.16	1.17	0.255
$\text{NO}_2$	-0.91	1.91	133.9	111.37	1.21	1.42/1.19	0.506

During the adsorption of molecules, except for  $\text{O}_2$  and  $\text{NO}_2$ , the surrounding of the vanadium atom changes from a square pyramid to an octahedral one. In the case of absorbed oxygen or nitrogen dioxide molecules, the vanadium atom formed the capped trigonal prismatic coordination because both oxygen or nitrogen and oxygen atoms interact with vanadium atoms.

For a detailed analysis of the change in the electronic configuration of the sorption site of the vanadium atom, we analyzed the density of electronic states (Figure 3) and electronic band structures (Figure S3 in Supplementary Materials). Despite the relatively high binding energy between the molecule and the substrate, molecule sorption does not always lead to a significant change in magnetic and electronic properties, as exemplified by the cases of CO,  $\text{NH}_3$ , and  $\text{H}_2\text{O}$  molecules sorption because their HOMO and LUMO states were located quite far away from the band gap of the  $\text{V}_3\text{S}_4$  nanosheet. Therefore, the  $\text{V}_3\text{S}_4$  monolayer is not appropriate for application as a detector of CO,  $\text{CO}_2$ ,  $\text{NH}_3$ , and  $\text{H}_2\text{O}$  molecules.

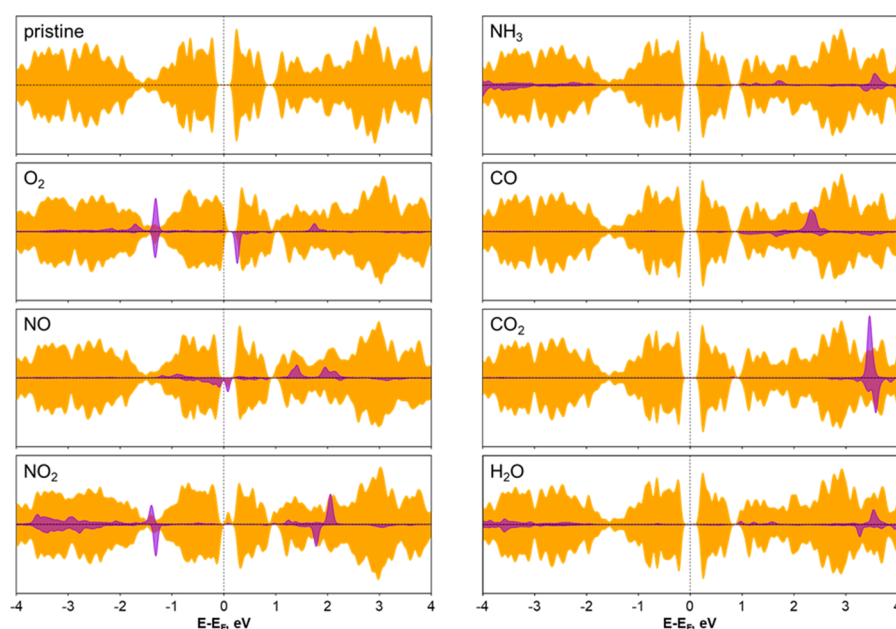


**Figure 3.** The density of electronic states of the  $\text{V}_3\text{S}_4$  monolayer before and after the adsorption of  $\text{CO}$ ,  $\text{CO}_2$ ,  $\text{H}_2\text{O}$ ,  $\text{O}_2$ ,  $\text{NH}_3$ ,  $\text{NO}$ , and  $\text{NO}_2$  gas molecules. Orange and violet colors denote the contribution from the  $\text{V}_3\text{S}_4$  monolayer and gas molecules, respectively. The Fermi level shifted to zero. The contribution from gas molecules was enlarged by 4 times for  $\text{CO}$ ,  $\text{CO}_2$ ,  $\text{O}_2$ ,  $\text{NO}$ , and  $\text{NO}_2$  molecules and by 20 times for the  $\text{H}_2\text{O}$  and  $\text{NH}_3$  molecules.

It is noteworthy that the HOMO and LUMO states of  $\text{NO}_2$  molecules are also located quite far from the band gap of  $\text{V}_3\text{S}_4$ , however, its sorption leads to the emergence of an unoccupied electronic state in the band gap of  $\text{V}_3\text{S}_4$  related mostly with vanadium atoms, which leads to a band gap reduction to 0.14 eV. At the sorbed configuration of  $\text{NO}_2$  molecules on the  $\text{V}_3\text{S}_4$  surface, the geometry of the molecule dramatically changed due to the electron donation from  $\text{V}_3\text{S}_4$  with filling of the antibonding orbital. This led to elongation of one of the N–O bonds to 1.42 Å. Such a feature indicates not only sensoric applications of  $\text{V}_3\text{S}_4$ , but can also be useful for the catalytic reduction of  $\text{NO}_2$  [60].

In contrast, at the adsorption of  $\text{O}_2$  and  $\text{NO}$  molecules, some electronic levels in the band gap were observed. The sorption of the oxygen molecules led to the appearance of unoccupied electronic states above the valence band maximum for one spin channel and band gap reduction to 0.24 eV. The molecule attracts electron density (0.473 e) due to high electronegativity to an antibonding orbital, which leads to an increase in O–O distance by 0.09 Å in comparison with the pure  $\text{O}_2$  molecule. This allows one to conclude about the viability of  $\text{V}_3\text{S}_4$  in catalytic applications in which it is required to lower the dissociation energy of molecular oxygen, for example, in oxygen reduction reactions [61,62].

In the case of  $\text{NO}$  molecule sorption, occupied states close to the valence band maximum and unoccupied states close to the Fermi level for one spin channel were observed, leading to the band gap reduction of 0.14 eV. The magnetic moment of the vanadium atom in a square pyramidal surrounding located under adsorbed  $\text{NO}$  molecule changes from  $2.14 \mu_B$  to  $1.67 \mu_B$ . Taking into account that the electric conductivity  $\sigma$  (which is the main parameter determining the sensitivity of the sensor) is proportional to  $\sigma \sim \exp(-E_g/k_B T)$  (where  $E_g$  is the band gap,  $k_B$  is the Boltzmann's constant, and  $T$  is the temperature), we can conclude that due to significant band gap reduction caused by the sorption of  $\text{NO}$  and  $\text{NO}_2$  molecules, the  $\text{V}_3\text{S}_4$  monolayer is a prospective material for  $\text{NO}$  and  $\text{NO}_2$  molecule detection. The detection of nitric oxide and nitric dioxide is of great importance for environmental protection as these harmful gases are emitted from the upstream of oil and gas production [63]. The development of novel materials that can be used both as sensors and catalysts for  $\text{NO}$  and  $\text{NO}_2$  reduction will positively affect sustainable development.

#### 4. Conclusions

In this work, we performed a variable-composition evolutionary search for new stable two-dimensional V–S monolayers with different  $U_{eff}$  values (from 0 to 4 eV) via the USPEX algorithm. The new 2D  $V_3S_4$  structure was found to be thermodynamically and dynamically stable, showing intriguing electronic and magnetic properties for sensing applications. We found that the  $V_3S_4$  monolayer exists in an antiferromagnetic ground state and shows semiconducting behavior with a band gap of 0.36 eV. These features signal that the  $V_3S_4$  monolayer can be used as a gas sensor for different gas agents. We proved this idea by calculating the energies of adsorption and electronic properties of  $V_3S_4$  with adsorbed CO,  $CO_2$ , NO,  $NO_2$ ,  $NH_3$ ,  $H_2O$ , and  $O_2$  molecules. Detailed analysis of the electronic properties of  $V_3S_4$  showed its prospective to be used as effective sensing materials for  $NO_2$  and NO gas molecules and as a material for catalytic applications in which it is required to lower the dissociation energy of  $O_2$ , for example, in the oxygen reduction reactions. The obtained results pave the way for using transition metal chalcogenide monolayers in gas sensors.

**Supplementary Materials:** The following supporting information can be downloaded at: <https://www.mdpi.com/article/10.3390/nano12050774/s1>; Figure S1: The atomic structures of predicted thermodynamically stable phases (except for  $V_3S_4$ ); Table S1: The lattice parameters of predicted V–S structures; Figure S2: Considered antiferromagnetic configurations for  $2 \times 1 \times 1$  supercell of the  $V_3S_4$  phase; Table S2: The energy difference between considered magnetic configurations and the most energetically favorable AFM10 configuration and absolute values of magnetic moment on vanadium atoms in square pyramidal ( $V_{sq\_pyr}$ ) and octahedral ( $V_{oct}$ ) surroundings; Figure S3: The most energetically favorable configuration of considered gas molecules ( $O_2$ , NO,  $NO_2$ ,  $NH_3$ , CO,  $CO_2$ , and  $H_2O$ ) on the  $V_3S_4$  surface and corresponding electronic band structures before and after the gas molecule adsorption. Spin up and down bands are shown by red and blue colors, respectively. The red, yellow, blue, brown, grey and green colors representing vanadium, sulfur, oxygen, carbon, nitrogen and hydrogen atoms are depicted, respectively

**Author Contributions:** Conceptualization, Z.I.P. and A.G.K.; Formal analysis, E.V.S. and A.M.M.; Investigation, I.V.C., E.V.S., H.A.Z., M.A.A., Y.S.M. and D.G.K.; Data curation, A.G.K.; Writing—original draft preparation, I.V.C.; Writing—review and editing, E.V.S., A.G.K., A.M.M. and Z.I.P.; Visualization, E.V.S.; Supervision, Z.I.P.; Funding acquisition, Z.I.P. All authors have read and agreed to the published version of the manuscript.

**Funding:** The reported study was funded by RFBR and SC RA, project No. 20-53-05009 Arm\_a and 20RF-185.

**Data Availability Statement:** Not applicable.

**Acknowledgments:** The authors thank Sergey Streltsov for the fruitful discussion and the Center for Information and Computing of Novosibirsk State University for computational resources.

**Conflicts of Interest:** The authors declare no conflict of interest.

#### References

- Shinde, P.V.; Rout, C.S. Magnetic gas sensing: Working principles and recent developments. *Nanoscale Adv.* **2021**, *3*, 1551–1568. [[CrossRef](#)]
- Kiani, M.; Rehman, M.U.; Tian, X.; Yakobson, B. Two-dimensional nanomaterials for the development of efficient gas sensors: Recent advances, challenges, and future perspectives. *Adv. Mater. Technol.* **2021**, *2101252*. [[CrossRef](#)]
- Lin, T.; Lv, X.; Hu, Z.; Xu, A.; Feng, C. Semiconductor metal oxides as chemoresistive sensors for detecting volatile organic compounds. *Sensors* **2019**, *19*, 233. [[CrossRef](#)] [[PubMed](#)]
- Zhang, J.; Liu, X.; Neri, G.; Pinna, N. Nanostructured materials for room-temperature gas sensors. *Adv. Mater.* **2016**, *28*, 795–831. [[CrossRef](#)] [[PubMed](#)]
- Liu, X.; Ma, T.; Pinna, N.; Zhang, J. Two-dimensional nanostructured materials for gas sensing. *Adv. Funct. Mater.* **2017**, *27*, 1702168. [[CrossRef](#)]
- Joshi, N.; Hayasaka, T.; Liu, Y.; Liu, H.; Oliveira, O.N.; Lin, L. A review on chemiresistive room temperature gas sensors based on metal oxide nanostructures, graphene and 2D transition metal dichalcogenides. *Microchim. Acta* **2018**, *185*, 213. [[CrossRef](#)]
- Matatagui, D.; Kolokoltsev, O.V.; Qureshi, N.; Mejia-Uriarte, E.V.; Saniger, J.M. A magnonic gas sensor based on magnetic nanoparticles. *Nanoscale* **2015**, *7*, 9607–9613. [[CrossRef](#)]

8. Sukhanova, E.; Visotin, M.A.; Popov, Z.I.; Sorokin, P.B. Stability and gas sensing properties of  $Ta_2X_3M_8$  ( $X = Pd, Pt; M = S, Se$ ) nanoribbons: A first-principles investigation. *Phys. Chem. Chem. Phys.* **2020**, *22*, 14651–14659. [CrossRef]
9. Ciprian, R.; Baratto, C.; Giglia, A.; Koshmak, K.; Vinai, G.; Donarelli, M.; Ferroni, M.; Campanini, M.; Comini, E.; Ponzoni, A. Magnetic gas sensing exploiting the magneto-optical kerr effect on  $ZnO$  nanorods/Co layer system. *RSC Adv.* **2016**, *6*, 42517–42521. [CrossRef]
10. Lin, G.; Makarov, D.; Schmidt, O.G. Magnetic sensing platform technologies for biomedical applications. *Lab Chip* **2017**, *17*, 1884–1912. [CrossRef]
11. Zheng, W.; Liu, X.; Xie, J.; Lu, G.; Zhang, J. Emerging van der Waals junctions based on TMDs materials for advanced gas sensors. *Coord. Chem. Rev.* **2021**, *447*, 214151. [CrossRef]
12. Zheng, W.; Xu, Y.; Zheng, L.; Yang, C.; Pinna, N.; Liu, X.; Zhang, J.  $MoS_2$  Van der Waals p–n junctions enabling highly selective room-temperature  $NO_2$  sensor. *Adv. Funct. Mater.* **2020**, *30*, 2000435. [CrossRef]
13. Zhao, R.; Wang, T.; Zhao, M.; Xia, C.; An, Y.; Wei, S.; Dai, X. External electric field and strains facilitated nitrogen dioxide gas sensing properties on 2D monolayer and bilayer  $SnS_2$  nanosheets. *Appl. Surf. Sci.* **2019**, *491*, 128–137. [CrossRef]
14. Zhao, R.; Wang, T.; An, Y.; Dai, X.; Xia, C.  $VS_2$  nanosheet as a promising candidate of recycle and reuse  $NO_2$  gas sensor and capturer: A DFT study. *J. Phys. Condens. Matter* **2021**, *33*, 165501. [CrossRef]
15. Ataca, C.; Şahin, H.; Ciraci, S. Stable, single-layer  $MX_2$  transition-metal oxides and dichalcogenides in a honeycomb-like structure. *J. Phys. Chem. C* **2012**, *116*, 8983–8999. [CrossRef]
16. Lv, R.; Robinson, J.A.; Schaaak, R.E.; Sun, D.; Sun, Y.; Mallouk, T.E.; Terrones, M. Transition metal dichalcogenides and beyond: Synthesis, properties, and applications of single- and few-layer nanosheets. *Acc. Chem. Res.* **2015**, *48*, 56–64. [CrossRef]
17. Shidpour, R.; Manteghian, M. A density functional study of strong local magnetism creation on  $MoS_2$  nanoribbon by sulfur vacancy. *Nanoscale* **2010**, *2*, 1429–1435. [CrossRef]
18. He, J.; Wu, K.; Sa, R.; Li, Q.; Wei, Y. Magnetic properties of nonmetal atoms absorbed  $MoS_2$  monolayers. *Appl. Phys. Lett.* **2010**, *96*, 082504. [CrossRef]
19. Wang, Z.; Zhao, K.; Li, H.; Liu, Z.; Shi, Z.; Lu, J.; Suenaga, K.; Joung, S.-K.; Okazaki, T.; Jin, Z.; et al. Ultra-narrow  $WS_2$  nanoribbons encapsulated in carbon nanotubes. *J. Mater. Chem.* **2010**, *21*, 171–180. [CrossRef]
20. Li, Y.; Zhou, Z.; Zhang, S.; Chen, Z.  $MoS_2$  nanoribbons: High stability and unusual electronic and magnetic properties. *J. Am. Chem. Soc.* **2008**, *130*, 16739–16744. [CrossRef]
21. Ma, Y.; Dai, Y.; Guo, M.; Niu, C.; Lu, J.; Huang, B. Electronic and magnetic properties of perfect, vacancy-doped, and nonmetal adsorbed  $MoSe_2$ ,  $MoTe_2$  and  $WS_2$  monolayers. *Phys. Chem. Chem. Phys.* **2011**, *13*, 15546–15553. [CrossRef]
22. Ma, Y.; Dai, Y.; Guo, M.; Niu, C.; Huang, B. Graphene adhesion on  $MoS_2$  monolayer: An ab initio study. *Nanoscale* **2011**, *3*, 3883–3887. [CrossRef] [PubMed]
23. Gao, D.; Xue, Q.; Mao, X.; Wang, W.; Xu, Q.; Xue, D. Ferromagnetism in ultrathin  $VS_2$  nanosheets. *J. Mater. Chem. C* **2013**, *1*, 5909–5916. [CrossRef]
24. Ma, Y.; Dai, Y.; Guo, M.; Niu, C.; Zhu, Y.; Huang, B. Evidence of the existence of magnetism in pristine  $VX_2$  monolayers ( $X = S, Se$ ) and their strain-induced tunable magnetic properties. *ACS Nano* **2012**, *6*, 1695–1701. [CrossRef] [PubMed]
25. Coelho, P.M.; Nguyen Cong, K.; Bonilla, M.; Kolekar, S.; Phan, M.-H.; Avila, J.; Asensio, M.C.; Oleynik, I.I.; Batzill, M. Charge density wave state suppresses ferromagnetic ordering in  $VSe_2$  monolayers. *J. Phys. Chem. C* **2019**, *123*, 14089–14096. [CrossRef]
26. Ma, Y.; Dai, Y.; Guo, M.; Niu, C.; Huang, B. Intriguing behavior of halogenated two-dimensional tin. *J. Phys. Chem. C* **2012**, *116*, 12977–12981. [CrossRef]
27. Zhong, M.; Li, Y.; Xia, Q.; Meng, X.; Wu, F.; Li, J. Ferromagnetism in  $VS_2$  nanostructures: Nanoflowers versus ultrathin nanosheets. *Mater. Lett.* **2014**, *124*, 282–285. [CrossRef]
28. Joseph, T.; Ghorbani-Asl, M.; Kvashnin, A.G.; Larionov, K.V.; Popov, Z.I.; Sorokin, P.B.; Krasheninnikov, A.V. Nonstoichiometric phases of two-dimensional transition-metal dichalcogenides: From chalcogen vacancies to pure metal membranes. *J. Phys. Chem. Lett.* **2019**, *10*, 6492–6498. [CrossRef]
29. Zhu, Q.; Xiao, Q.; Zhang, B.; Yan, Z.; Liu, X.; Chen, S.; Ren, Z.; Yu, Y.  $VS_4$  with a chain crystal structure used as an intercalation cathode for aqueous Zn-ion batteries. *J. Mater. Chem. A* **2020**, *8*, 10761–10766. [CrossRef]
30. Kozlova, M.N.; Mironov, Y.V.; Grayfer, E.D.; Smolentsev, A.I.; Zaikovskii, V.I.; Nebogatikova, N.A.; Podlipskaya, T.Y.; Fedorov, V.E. Synthesis, crystal structure, and colloidal dispersions of vanadium tetrasulfide ( $VS_4$ ). *Chem. Eur. J.* **2015**, *21*, 4639–4645. [CrossRef]
31. Knecht, M.; Ebert, H.; Bensch, W. Electronic and magnetic properties of  $V_5S_8$ . *J. Phys. Condens. Matter* **1998**, *10*, 9455–9463. [CrossRef]
32. Kitaoka, Y.; Yasuoka, H. NMR investigations on the spin fluctuations in itinerant antiferromagnets. II.  $V_3S_4$  and  $V_5S_8$ . *J. Phys. Soc. Jpn.* **1980**, *48*, 1949–1956. [CrossRef]
33. Jellinek, F. Structural study of vanadium sulfides. *Rev. Chim. Minér.* **1974**, *11*, 624–636.
34. Kawada, I.; Nakano-Onoda, M.; Ishii, M.; Saeki, M.; Nakahira, M. Crystal structures of  $V_3S_4$  and  $V_5S_8$ . *J. Solid State Chem.* **1975**, *15*, 246–252. [CrossRef]
35. Materials Project. Available online: <https://materialsproject.org/> (accessed on 20 June 2021).
36. Bensch, W.; Ebert, H. The electronic bandstructure of hexagonal  $V_3S_4$  isotypic with  $Nb_3S_4$ . *Solid State Commun.* **1994**, *89*, 235–238. [CrossRef]

37. Oganov, A.R.; Glass, C.W. Crystal structure prediction using ab initio evolutionary techniques: Principles and applications. *J. Chem. Phys.* **2006**, *124*, 244704. [[CrossRef](#)]
38. Oganov, A.R.; Lyakhov, A.O.; Valle, M. How evolutionary crystal structure prediction works—And why. *Acc. Chem. Res.* **2011**, *44*, 227–237. [[CrossRef](#)]
39. Lyakhov, A.O.; Oganov, A.R.; Stokes, H.T.; Zhu, Q. New developments in evolutionary structure prediction algorithm USPEX. *Comput. Phys. Commun.* **2013**, *184*, 1172–1182. [[CrossRef](#)]
40. Hohenberg, P.; Kohn, W. Inhomogeneous electron gas. *Phys. Rev.* **1964**, *136*, B864–B871. [[CrossRef](#)]
41. Kohn, W.; Sham, L.J. Self-consistent equations including exchange and correlation effects. *Phys. Rev.* **1965**, *140*, A1133–A1138. [[CrossRef](#)]
42. Perdew, J.P.; Burke, K.; Ernzerhof, M. Generalized gradient approximation made simple. *Phys. Rev. Lett.* **1996**, *77*, 3865–3868. [[CrossRef](#)] [[PubMed](#)]
43. Kresse, G.; Hafner, J. Ab initio molecular dynamics for liquid metals. *Phys. Rev. B* **1993**, *47*, 558–561. [[CrossRef](#)]
44. Kresse, G.; Hafner, J. Ab initio molecular-dynamics simulation of the liquid-metal—Amorphous-semiconductor transition in germanium. *Phys. Rev. B* **1994**, *49*, 14251–14269. [[CrossRef](#)] [[PubMed](#)]
45. Kresse, G.; Furthmüller, J. Efficient iterative schemes for ab initio total-energy calculations using a plane-wave basis set. *Phys. Rev. B* **1996**, *54*, 11169–11186. [[CrossRef](#)] [[PubMed](#)]
46. Kresse, G.; Furthmüller, J. Efficiency of ab-initio total energy calculations for metals and semiconductors using a plane-wave basis set. *Comput. Mater. Sci.* **1996**, *6*, 15–50. [[CrossRef](#)]
47. Blöchl, P.E. Projector augmented-wave method. *Phys. Rev. B* **1994**, *50*, 17953–17979. [[CrossRef](#)]
48. Monkhorst, H.J.; Pack, J.D. Special points for Brillouin-zone integrations. *Phys. Rev. B* **1976**, *13*, 5188–5192. [[CrossRef](#)]
49. Anisimov, V.I.; Zaanen, J.; Andersen, O.K. Band theory and Mott insulators: Hubbard U instead of Stoner I. *Phys. Rev. B* **1991**, *44*, 943–954. [[CrossRef](#)]
50. Dudarev, S.L.; Botton, G.A.; Savrasov, S.Y.; Humphreys, C.J.; Sutton, A.P. Electron-energy-loss spectra and the structural stability of nickel oxide: An LSDA + U study. *Phys. Rev. B* **1998**, *57*, 1505–1509. [[CrossRef](#)]
51. Grimme, S.; Antony, J.; Ehrlich, S.; Krieg, H. A consistent and accurate ab initio parametrization of density functional dispersion correction (DFT-D) for the 94 elements H–Pu. *J. Chem. Phys.* **2010**, *132*, 154104. [[CrossRef](#)]
52. Togo, A.; Tanaka, I. First principles phonon calculations in materials science. *Scr. Mater.* **2015**, *108*, 1–5. [[CrossRef](#)]
53. Togo, A.; Oba, F.; Tanaka, I. First-principles calculations of the ferroelastic transition between rutile-type and CaCl<sub>2</sub>-type SiO<sub>2</sub> at high pressures. *Phys. Rev. B* **2008**, *78*, 134106. [[CrossRef](#)]
54. Ganose, A.M.; Jackson, A.J.; Scanlon, D.O. Sumo: Command-line tools for plotting and analysis of periodic\*ab initio\* calculations. *J. Open Source Softw.* **2018**, *3*, 717. [[CrossRef](#)]
55. Zhuang, H.L.; Hennig, R.G. Stability and magnetism of strongly correlated single-layer VS<sub>2</sub>. *Phys. Rev. B* **2016**, *93*, 054429. [[CrossRef](#)]
56. Esters, M.; Hennig, R.G.; Johnson, D.C. Dynamic instabilities in strongly correlated VSe<sub>2</sub> monolayers and bilayers. *Phys. Rev. B* **2017**, *96*, 235147. [[CrossRef](#)]
57. Bensch, W.; Koy, J. Structure of hexagonal V<sub>3</sub>S<sub>4</sub> determined at three different temperatures. *Acta Crystallogr. Sect. C Cryst. Struct. Commun.* **1993**, *49*, 1133–1135. [[CrossRef](#)]
58. Bader, R.F. Atoms in molecules. *Acc. Chem. Res.* **1985**, *18*, 9–15. [[CrossRef](#)]
59. Henkeman, G.A.; Arnaldsson, A.; Jónsson, H. A fast and robust algorithm for Bader decomposition of charge density. *Comput. Mater. Sci.* **2006**, *36*, 354–360. [[CrossRef](#)]
60. Wang, X.; Du, X.; Yang, G.; Xue, J.; Chen, Y.; Zhang, L. Chemisorption of NO<sub>2</sub> on V-based SCR catalysts: A fundamental study toward the mechanism of “Fast SCR” reaction. *J. Phys. Chem. C* **2019**, *123*, 20451–20458. [[CrossRef](#)]
61. Sun, H.; Wang, M.; Zhang, S.; Liu, S.; Shen, X.; Qian, T.; Niu, X.; Xiong, J.; Yan, C. Boosting oxygen dissociation over bimetal sites to facilitate oxygen reduction activity of zinc-air battery. *Adv. Funct. Mater.* **2021**, *31*, 2006533. [[CrossRef](#)]
62. Wan, H.; Jensen, A.W.; Escudero-Escribano, M.; Rossmeisl, J. Insights in the oxygen reduction reaction: From metallic electrocatalysts to diporphyrins. *ACS Catal.* **2020**, *10*, 5979–5989. [[CrossRef](#)]
63. Gonzalez, D.J.X.; Francis, C.K.; Shaw, G.M.; Cullen, M.R.; Baiocchi, M.; Burke, M. Upstream oil and gas production and ambient air pollution in California. *Sci. Total Environ.* **2022**, *806*, 150298. [[CrossRef](#)] [[PubMed](#)]